On the formation of "Fish-scale" morphology with curved grain interfacial microstructures during selective laser melting of dissimilar alloys

Preprint *in* Acta Materialia · September 2021

DOI: 10.1016/j.actamat.2021.117331

CITATIONS
60

READS
503

4 authors, including:

Liming Yao
Nanyang Technological University
29 PUBLICATIONS **318** CITATIONS

SEE PROFILE

Sheng Huang
Massachusetts Institute of Technology
25 PUBLICATIONS **1,046** CITATIONS

SEE PROFILE

Z. M. Xiao
Nanyang Technological University
195 PUBLICATIONS **3,296** CITATIONS

SEE PROFILE

On the formation of "Fish-scale" morphology with curved grain interfacial microstructures during selective laser melting of dissimilar alloys

Liming Yao[1], Sheng Huang[1], Upadrasta Ramamurty[1,2], Zhongmin Xiao[1]*

[1]School of Mechanical and Aerospace Engineering, Nanyang Technological University, 50 Nanyang Avenue, 639798, Singapore.

[2]Institute of Materials Research and Engineering, Agency for Science, Technology and Research (A*STAR), Singapore 138634.

Abstract: For successful fabrication of components using additive manufacturing techniques such as powder bed fusion (PBF), directed energy deposition, and laser cladding of an alloy on to a substrate of a dissimilar one, an interpenetrating interface morphology is essential for a good interface strength. The physical mechanisms behind the formation of different solidified interface morphologies after single track laser PBF of Inconel 718 powders on to the 316L austenitic stainless stress substrate were investigated by recourse to numerical simulations, which combine micron-scale fluid dynamics and solidification protocols with nanosecond-level thermal diffusion processes. These were complemented with parametric experiments to verify the simulations. Results show that an interface with the "fish scale" morphology can occur under certain combinations of process parameters, and because of the combined actions of recoil pressure, Marangoni forces, surface tension and melt pool shape. Three distinct morphologies that depend on the melt pool width and depth are identified and the interfacial areas for each of them are computed. The influence of the processing conditions that not only dictate the geometric parameters of the melt pool but also the degree of alloying and the resulting grain morphology within the interface microstructure were elucidated.

Keywords: Additive manufacturing; Laser deposition; Interface; Heat flow and solidification; Computer simulations.

* Corresponding author.

E-mail address: mzxiao@ntu.edu.sg (Z.M. Xiao).

1. INTRODUCTION

Additive manufacturing (AM) of metallic components offers many advantages over conventional manufacturing methods and hence is being researched vigorously. The most widely explored AM technique is the selective fusing of powder beds (PBF)—line-by-line and layer-by-layer—using either lasers (LPBF) or e-beams (EPBF) to build the desired 3D object [1]. These techniques can also be utilized to fabricate components with continuous compositional gradients and join or clad dissimilar metals/alloys. Achieving these is challenging with PBF technologies in comparison to the directed energy deposition (DED) processes, but have been on the rise due to PBF's ability to build parts with higher intricacy and finer details. Hence, innovative solutions had been proposed for PBF systems to achieve compositionally dissimilar powder spreading in a single build process [2, 3, 4, 5, 6, 7]. Exploitation of these would enhance the versatility of AM substantially. However, imparting a strong metallurgical bond between the different metals that are being fused together is a key challenge as the differences in their thermo-physical and chemical properties may lead to weak interfaces [8, 9]. Such interfaces could act as the 'weak links' in the structure when it comes to the performance limiting the mechanical integrity and reliability of the fabricated part [10, 11, 12]. Since melting and subsequent solidification of the powders occurs rapidly during PBF [13], substantial residual stresses are intrinsic to these processes; such stresses can themselves aid in the detachment of the deposited layers [14]. Hence, a detailed understanding about the morphology of the interface between dissimilar alloys and the microstructural development at it during LPBF/EPBF or direct energy deposition is essential. However, gaining such an insight in a three-dimensional space is difficult through direct experimental observation, while on the other hand simulating the interface morphology of dissimilar alloys needs to consider the complex interplay between various physical processes (rapid melting and subsequent solidification of powders and associated thermal and molten fluid fields that are highly transient, etc.) [15, 16, 17, 18]. Therefore, the evolution of the three-dimensional morphology of the dissimilar alloy interface has not been presented hitherto [19, 20].

The interface morphologies, microstructures, and mechanical properties of the laser cladded dissimilar metals (LCDM) were extensively explored via the experimental route [21, 22, 23, 24], albeit from two-dimensional point of view. Some examples of the investigated alloys include Ti-based (Ti6Al4V/316 [25], Ti6Al4V/invar [9]), Fe-based (316L/Cu [26], Inconel625/316L [27]), and other (Invar 36/V [28], W/Cu [29], Cu10Sn/PA11 [30]) alloys. Strictly speaking, the interface

comprises of a region where dissimilar metals interdiffusion and form a region of intermediate composition, which could result in the formation of brittle secondary phase such as intermetallic compound and amorphous phase. This then leads to a major problem where cracking at the interface occurs due to the tensile residual stresses generated during the PBF process [31, 32, 33]. Should the clad interface survives the manufacturing process, strain localization at the brittle intermediate phase led to premature cracking and failure during mechanical tensile loading. In a prior study, it was shown that a straight interface is more detrimental (as compared to that of a curved one) as there is no barrier to stop crack propagation along the transition region [7]. In order to reduce such failure, a strong metallurgically bonded, interwoven interface that increases the specific surface area of it is essential [34, 35], which will also be useful to deprive the interface of an easy path for cracking. To realize such interfaces, detailed understanding of the solidification process through simulations under the prevailing PBF conditions is the key.

In the context of metal additive manufacturing, computational fluid dynamics (CFD) methods are extensively utilized to understand the physics of melting, solidification, evaporation, condensation and multiphase flow of a single alloy so as to optimize the quality of the printed parts [36, 37, 38, 39, 40]. However, such studies on dissimilar alloy PBF are sparse. Recently, Gu et al. [20] conducted CFD studies for selective laser melting of Cu10Sn alloy powder onto austenitic stainless steel 316L substrate. Since the laser absorptivity of the Cu10Sn powders is low (around 0.03), the heat conduction mode of melting is dominant. They found that the phase migration at the interface is related to the convection inside the melt pool, which helps the miscibility of the two alloys. In a subsequent work, Sun et al. took the miscibility between two alloys into account and simulated laser powder bed fusion processes of Cu10Sn powders on IN718 substrate [41]. Due to the heat conduction mode of melting with marginal penetration into the substrate, the formation of complex interlayer interface is limited by the availability of dissimilar materials in the melt pool. Consequently, melting dominated by the keyhole penetration through the interface between two alloys and associated morphological changes of the interface could not be captured through these modeling efforts.

In the present work, a multi-physics model that combines micron-scale fluid dynamics with nanosecond-level thermal diffusion processes to capture the thermal interactions between the ambient gases and alloys is utilized to simulate and then examine in detail the formation of microstructurally complex interface during LPBF of two dissimilar alloys. The simulation

predictions are validated with the single track LPBF experiments, to identify the conditions that would favor the formation of distinct interpenetrating interfaces with the 'fish scale' morphologies.

2. MELT FLOW MODELLING

The simulation model is established based on computational fluid dynamics and multiphase flow methods, which can suitably capture the melt pool dynamics of dissimilar alloys during the LPBF process. The volume of fluid (VOF) method is used to capture the gas/powder, gas/substrate, and powder/substrate interfaces. The model is customized based on the process conditions, accounting for the buoyant flow, Marangoni convection, vapor recoil pressure, and heat radiation. This model is not new, in which the same model had been used for the study of dissimilar alloys such as 316L / Cu10Sn by Gu et al. [20]. Sun et al. furthered the model by incorporating miscibility of dissimilar alloys for the study of IN718 / Cu10Sn. However, these studies did not perform sufficient validation studies to substantiate the accuracy of the model [41]. The following assumptions were introduced to simplify the model: (1) Newtonian and incompressible fluid with laminar flow was assumed [20], (2) the enthalpy-porosity technique introduced by Voller et al. [42] was adopted to simulate the alloy melting and solidification process, (3) mass loss due to vaporization was not included in the model [43], (4) Effects of small disturbances in the fields (e.g. dispersion fluxes, supercooling of the liquid, etc.) are neglected [42], (5) Homogeneous and isotropic properties in the phases, and thermodynamic equilibrium at the solid-liquid interface, and (6) the physics of chemical diffusion is not included. Instead, the mixing of dissimilar alloys occurs only in the interface cells and the resultant thermophysical parameters of the interface cells were estimated by the method of constituent weighted average.

At any instance, the volume fraction (α) of each phase in the fluid element should satisfy the following relationship:

$$\alpha_g + \alpha_p + \alpha_s = 1 \quad , \tag{1}$$

where the subscripts 'g', 'p' and 's' refer to gas, powder, and substrate, respectively. The properties of the mixture phase ($\bar{\phi}$) are evaluated by the weighted average of the constituents (ϕ):

$$\bar{\phi} = \alpha_g \phi_g + \alpha_p \phi_p + \alpha_s \phi_s \quad , \tag{2}$$

The interface cells located in between the two dissimilar alloys have intermediate composition of the two. As such, the solidus temperature $T_{s,m} = (\alpha_p T_{s,p} + \alpha_s T_{s,s})/(\alpha_p + \alpha_s)$ and

liquidus temperature $T_{\mathrm{l,m}} = (\alpha_{\mathrm{p}} T_{\mathrm{l,p}} + \alpha_{\mathrm{s}} T_{\mathrm{l,s}})/(\alpha_{\mathrm{p}} + \alpha_{\mathrm{s}})$ were correspondingly obtained based on the compositional weighted average.

Meanwhile, a temperature dependent variable γ is employed to represent the solid or liquid state of the alloy cells, described as:

$$\gamma_{(j)} = \begin{cases} 0 & T < T_{\mathrm{s},(j)} \\ \frac{T - T_{\mathrm{s},(j)}}{T_{\mathrm{l},(j)} - T_{\mathrm{s},(j)}} & T_{\mathrm{s},(j)} \le T \le T_{\mathrm{l},(j)} \\ 1 & T_{\mathrm{l},(j)} < T \end{cases}, \tag{3}$$

where $T_{\mathrm{s},(j)}$ and $T_{\mathrm{l},(j)}$ are the solidus and liquidus temperatures, respectively. The subscript j can be replaced by p, s, and m to represent the powder, the substrate and the dissimilar alloy interface cell, respectively. T is the temperature of the computational domain. The volume fractions of unmelted and molten powder are $\alpha_{\mathrm{p}}(1\text{-}\gamma_{\mathrm{p}})$ and $\alpha_{\mathrm{p}}\gamma_{\mathrm{p}}$, respectively. The volume fractions of unmelted and molten substrates are $\alpha_{\mathrm{s}}(1\text{-}\gamma_{\mathrm{s}})$ and $\alpha_{\mathrm{s}}\gamma_{\mathrm{s}}$, respectively. Likewise, the volume fractions of unmelted and molten alloy are $(\alpha_{\mathrm{p}}+\alpha_{\mathrm{s}})(1\text{-}\gamma_{\mathrm{s}})$ and $(\alpha_{\mathrm{p}}+\alpha_{\mathrm{s}})\gamma_{\mathrm{s}}$ in the dissimilar alloy interface cell, respectively. The alloy material properties in the cell can be expressed as:

$$(\alpha_{\mathrm{p}} + \alpha_{\mathrm{s}})\phi_{(j)} = (\alpha_{\mathrm{p}}\phi_{\mathrm{s,p}} + \alpha_{\mathrm{s}}\phi_{\mathrm{s,s}})(1\text{-}\gamma_{(j)}) + (\alpha_{\mathrm{p}}\phi_{\mathrm{l,p}} + \alpha_{\mathrm{s}}\phi_{\mathrm{l,s}})\gamma_{(j)} \tag{4}$$

where $\phi_{\mathrm{s,p}}$, $\phi_{\mathrm{l,p}}$ are the properties of the powder in the solid and molten states, and $\phi_{\mathrm{s,s}}$, $\phi_{\mathrm{l,s}}$ are the properties of the solid and molten substrate, respectively.

In the above model, the energy absorption and dissipation, interface force transformation processes all occur on the interface cell. Therefore, it is important to accurately capture the gas/powder and the gas/substrate interface cells, and the powder/substrate cell. The interface cells are identified by using the volume fraction of alloy phase $(\alpha_{\mathrm{p}}, \alpha_{\mathrm{s}})$. A cell is considered as an interface cell when it satisfies the following conditions:

$$\begin{cases} \alpha_{\mathrm{p}} = \alpha_{\mathrm{s}} \ge 0.5 \\ |\alpha_{\mathrm{p}}| = |\alpha_{\mathrm{s}}| \ge {}^{\varepsilon}/_{\Delta x} = {}^{0.05}/_{\Delta x} \end{cases}, \tag{5}$$

where Δx is the cell width (or the 'grid size') and ε is a small arbitrary number (0.05). Firstly, only those cells containing alloy phases $\alpha_{\mathrm{p}} = \alpha_{\mathrm{s}} \ge 0.5$ will absorb power during laser scan process. Secondly, as for VOF method, the gradient of powder α_{p} and substrate α_{s} volume fraction is inversely proportional to Δx and is non-zero only at the interface. The tracking of the interface is accomplished by solving the continuity equation for the phase volume fractions.

The conservation equations for mass, momentum and energy can be expressed in sequence as [41, 43]:

$$\frac{\partial \rho}{\partial t} + \nabla \cdot (\rho \vec{u}) = 0 \quad , \tag{6}$$

$$\frac{\partial (\rho \vec{u})}{\partial t} + \nabla \cdot (\rho \vec{u} \otimes \vec{u}) = -\nabla P + \rho \vec{g} + \nabla \cdot (\mu \nabla \vec{u}) + \vec{f}_{\mathrm{d}} + \vec{f}_{\mathrm{t}} + \vec{f}_{m} + \vec{f}_{\mathrm{r}} \quad , \tag{7}$$

$$\frac{\partial (\rho C_{\mathrm{p}} T)}{\partial t} + \nabla \cdot \left(\rho \vec{u} C_{\mathrm{p}} T\right) = -\frac{\partial (\rho H_{\mathrm{m}})}{\partial t} - \nabla \cdot (\rho \vec{u} H_{\mathrm{m}}) + \nabla \cdot (k \nabla T) + q_{\mathrm{V}} + q_{\mathrm{rad}} + q_{\mathrm{L}} \quad , \tag{8}$$

where ρ is the volume average density, $\vec{u}$ is the flow velocity, P is the pressure, $\vec{g}$ is the acceleration of gravity, μ is the dynamic viscosity, $\vec{f}_{\mathrm{d}}$ is the momentum sink term used to account for the pressure drop due to the solidification of the molten alloy in the liquid-solid mushy zone, $\vec{f}_{\mathrm{t}}$ is the surface tension force, $\vec{f}_{m}$ is the Marangoni force, $\vec{f}_{\mathrm{r}}$ is the recoil pressure, C_{p} is the specific heat capacity, H_{m} is the latent heat of melting, k is the thermal conductivity, q_{v} is the heat loss due to vaporization of the alloy, q_{rad} is the radiation heat released into the ambient environment, and q_{L} is a simplified ray-trace Gaussian heat source [41, 44]. The source of surface tension and Marangoni force assume the following form [43]:

$$\vec{f}_{\mathrm{t}} = \sigma \kappa \vec{n} \left|\nabla \alpha_{(i)}\right| \frac{2\bar{\rho}}{\rho_{\mathrm{m}} + \rho_{\mathrm{g}}} \quad , \tag{9}$$

$$\vec{f}_{\mathrm{m}} = \frac{d\sigma}{dT} (\nabla T - \vec{n}(\vec{n} \cdot \nabla T)) \left|\nabla \alpha_{(i)}\right| \frac{2\bar{\rho}}{\rho_{\mathrm{m}} + \rho_{\mathrm{g}}} \quad , \tag{10}$$

where $\vec{n}$ is the unit normal vector at the interface, κ is the curvature of the interface. $\alpha_{(i)}$ is the volume fraction in the interfacial cell of the alloy. The subscript i can take the values of either 1 or 2, representing the powder and substrate, respectively. $|\nabla \alpha_{(i)}|$ is used to transform the interfacial force into a volumetric force. $2\bar{\rho}/(\rho_{\mathrm{m}} + \rho_{\mathrm{g}})$ is used to redistribute the interfacial force toward the heavier phase (the alloy phase). $d\sigma/dT$ describes the temperature coefficient of surface tension. σ is the surface tension coefficient of the molten alloy, including σ_{p}, σ_{s} and σ_{m}. Among them, σ_{p} and σ_{s} can be obtained from the literature [43, 45, 46], and the curve of surface tension with temperature is shown in Fig. S1. The surface tension σ_{s} between SS316L and air as well as the surface tension σ_{p} between IN718 and air are known. However, the surface tension between molten SS316L and IN718 has not been reported yet, so the surface tension between SS316 and IN718 is simplified here. The surface tension σ_{m} between SS316L and IN718 is considered by the interfacial cell and is estimated through the relation, $\sigma_{\mathrm{m}} = \left|\alpha_{\mathrm{p}}\sigma_{\mathrm{p}} - \alpha_{\mathrm{s}}\sigma_{\mathrm{s}}\right|/(\alpha_{\mathrm{p}} + \alpha_{\mathrm{s}})$.

The fluid equations were solved using the commercial computational fluid dynamics software ANSYS FLUENT. A user-defined function (UDF) was compiled for the purpose of additional source items required for multi-alloy LPBF simulation. The volume of the calculation domain is 1500 μm × 450 μm × 200 μm. Based on a grid independence test, the mesh size was set as 1.5 μm, and the maximum time step was set as 1.2×10^{-7} s. Thermo-physical properties of 316L and IN718 utilized are collected from published literature and are listed Table S1 in the supplementary material.

It is important to emphasize here that interdiffusion between IN718 and 316L during LPBF process does occur to a certain degree. Strictly, a sharp interface between the two alloys after the melting process is unlikely. Nevertheless, the simulations performed here using a simplified model, do provide insights into the spatial distribution of dissimilar alloys and the flow characteristics of the melt pools, which is the objective of this study.

3. MATERIALS AND EXPERIMENTS

The validity of the simulation model was ascertained by recourse to single track L-PBF experiments on Inconel 718 deposited on 316L austenitic stainless steel (referred to as IN718 and 316L here after) substrate. Their respective nominal chemical compositions (in wt.%) are: 16–18% Cr, 10–14% Ni, 2–3% Mo, < 0.03% C, < 1% Si, < 2% Mn, < 0.045% P, < 0.03% S, < 0.1% N, balance Fe and 17–21% Cr, 50–55% Ni, 2.8–3.3% Mo, < 0.08% C, < 0.35% Si, < 0.35% Mn, < 0.015% P, < 0.015% S, < 0.1%N, 4.75–5.5% Nb, 0.65–1.15% Ti, 0.2–0.8% Al, < 1.0% Co, < 0.006% B, < 0.3% Cu, < 0.05% Ta, balance Fe. A 280 HL LPBF machine (SLM Solutions Group AG) equipped with 1064 nm wavelength fiber laser with a focus diameter of 80 μm, Gaussian beam profile, and maximum power capacity of 400 W, was used. The fabrication was performed in an argon filled chamber of < 500 ppm oxygen to minimize oxidation and contamination. Prior to the scans, the powder re-coater blade was moved vertically by 45 μm above the wrought 316L base plate. A 45 μm thick layer of IN718 powder (size distribution range: 20 to 45 μm) was then spread evenly on the base plate with the re-coater blade. Thereafter, single track laser scans were performed to fuse the powder onto the base plate, with various combinations of laser power (L) and velocity (V), over a track of length 50 mm each. While L was varied between 100 and 300 W (with 100 W increments), V was varied between 300 and 2100 mm/s (with increments of 300 mm/s).

After the scans, the tracks were cross-sectioned at various locations via electro-discharge machining to examine the microstructures. The cut samples were ground and polished with successively finer diamond particle suspensions, before a final polish with 0.04 μm colloidal silica to achieve mirror finish. To examine the compositional distribution across the polished cross-sections, energy dispersive X-Ray spectroscopy (EDS) mapping was then conducted with a maximum step size of 0.14 μm. Electron backscattering diffraction (EBSD) mapping was done with a scanning step size of 0.4 μm to obtain the grain orientation maps. The EDS and EBSD mapping were conducted with a field emission scanning electron microscope (FESEM, JEOL 7800F Prime, JEOL, Japan) equipped with an EDS detector (X-Max EDS system, Oxford Instruments, UK) and an EBSD detector (Symmetry, Oxford Instruments, UK).

4. RESULTS

4.1 Topology, depth, and width of the melt pool

Since the single track LPBF simulations and experiments were performed on IN718 powders on the 316L substrate under identical conditions, their results are presented together in the following. Fig. 1 shows a representative image of the simulated single track. It illustrates various cross-sections that are utilized to analyze the characteristics of melt pool flow and alloy composition distribution and viewing angles. Cross-section A-A is parallel to the scan and build direction, located at the middle line of the melt pool width. Cross-sections B-B to D-D are in the melt track range and perpendicular to the scan direction while parallel to the build direction; they divide the length of the scanned length into four equal parts. Cross-section E-E is in the solidified track and perpendicular to the scan direction while parallel to the build direction.

The topography of a single track is illustrated in Fig. 2. Stereo microscopic observation of the single track (viewed from the direction I in Fig. 1) reveals protruding “droplet” formation of the melt pool at the beginning of it [43]. Both the width and height the track at the middle are relatively uniform, while a spoon-like cave-in is observed at the end of the track [47]. Different physical parameters, such as the width (W_m), depth (D_m) and aspect ratio D_m / W_m of the solidified tracks, are highlighted on Figs. 1 and 2. While D_m is the distance from the bottom of the melt pool to the top of the substrate, W_m is the track width on the top surface of the substrate and perpendicular to the scan direction. Variations of D_m, W_m and D_m / W_m with V at three different L are displayed in Fig. 3. An agreement between the experimental and simulated values of D_m and W_m validates the

simulation methodology. (See Table S2 and movies S3 and S6 in the supplementary material for further details.) It is seen from Figs. 3(a) and (b) that both D_m and W_m decrease asymptotically with V for all L. For a given V, D_m values obtained L of 200 and 300 W appear to overlap and are much higher than those noted for L = 100 W. In contrast, the enhancements in W_m with L are more evenly spaced. These observations imply that increasing the laser power at a fixed scan velocity is more effective in widening the melt pool, once some critical power input is exceeded, rather than deepening it. Further, D_m / W_m values obtained for L = 200 and 300 W appear to overlap and are much higher than those noted for L = 100 W for a given V [see Fig. 3(c)]. It shows that the melt pool aspect ratio of L = 200 and 300 W is similar for all V, which is higher than when L = 100 W. The observation is different from previous studies when a single alloy component was used, where D_m/W_m increases with L despite a diminishing return in terms of the volume of the material that is fused [48]. The reason behind the phenomena is unclear but does not affect the understanding on the interface forming mechanism.

Due to the presence of multiple alloys, the resultant melt flow characteristics can be different from the case of a single alloy, hence a closer observation in this aspect was done with L = 200 W and V = 900 mm/s single track presented here. The melt pool surface tension characteristic is an important factor that affects the resultant melt flow and can be obtained based on the thermal history. Of which the T_{ep} = 1801 K and T_{es} = 2400 K are the temperature of IN718 and 316L at the transition of the surface tension gradient [43, 45, 46], where the variation of surface tension with temperature can be seen in Fig. S1. Based on the melt pool surface tension characteristic, the melt flow analysis can be divided into four regions namely the keyhole region, and the negative, mixed and positive surface tension gradient regions. These regions, along with melt flow characteristic and distribution of different alloys are illustrated in Fig. 4(a). Meanwhile, the characteristic of surface tension gradient is shown in Fig. 4(b) and the associated surface temperature characteristics are shown in Fig. 4(c).

In the keyhole region, the temperature range ranges from 3090K to 3303K (the boiling point of 316L and IN718). The alloy evaporation in the keyhole region brings about violent but chaotic heat transfer, resulting in temperature fluctuations with positive and negative temperature gradients [Fig. 4(c)]. Due to the fast laser scanning of LPBF, the recoil pressure effect is not always parallel to the build direction, but towards the negative surface tension gradient region behind the keyhole and pushes the melt in the direction opposite to the scanning direction [Fig. 4(a)].

In the negative surface tension gradient region, the temperature ranges from 2400 K to 3090 K, both IN718 and 316L have not reached T_{ep} and T_{es} in this region [Fig. S1], and the collectively negative surface tension gradient is reflected in Fig. 4(b). The surface temperature and temperature gradient generally decrease in the direction away from the keyhole [Fig. 4(c)]. In this case, the Marangoni force should have the tendency to drive the melt flow in a counterclockwise fashion, but the recoil pressure pushes the melt altogether in the direction opposite to the scan direction [Fig. 4(a)].

In the mixed surface tension gradient region, the temperature ranges from 1801 K to 2400 K. 316L went under T_{es} but IN718 remains above T_{ep} [Fig. S1], hence the surface tension gradients of IN718 and 316L are negative and positive respectively [as shown in Fig. 4(b) at the mixed blue and red region]. The alloy distribution in this region is staggered and complex, where the positive and negative surface tension gradients correspond to the alloy distribution. The Marangoni forces generated by the positive and negative surface tension gradients offset each other in different directions. In addition, the alloy surface temperature gradient is nearly zero in this region [Fig. 4(c)], hence the driving force for the melt flow is due to the push by the negative surface tension gradient region and pull by the positive surface tension region, causing the melt to move in the opposite direction to the scan direction [Fig. 4(a)]. This net flow also explains the hump as seen on the T_{ep} and T_{es} isotherms [Fig. 4(b)].

In the positive surface tension gradient region, the temperature ranges from 1533 K (IN718 solidus temperature) to1801 K, where the temperature of IN718 falls below T_{ep} [Fig. S1]. At this point, the surface tension gradient of the entire region is positive [Fig. 4(b)], which results in a typical Marangoni force that drives the melt flow in a clockwise fashion [Fig. 4(a)].

It is worth noting that the melt pool flow trend and temperature gradient distribution of a single alloy (IN718 or 316L) are similar to the results observed in our study of dissimilar alloys [43, 45]. However, comparing to a single alloy melt pool, the temperature gradient distribution in the mixing region of the dissimilar alloy melt pool is complicated and may require special attention in the future.

An examination of the solidified interface between the two alloys, from the viewing angle II depicted in Fig. 1, reveals that for some combinations of the scan parameters, the morphology of the contour features interface, which are extracted from the simulation results, resemble those of a "fish scale", with interpenetrating layers of IN718 and 316L, as shown in Fig. 5 and movies S1

and S4. Since such interpenetrating network feature is desirable for a strong bond between the dissimilar alloys that are either additively manufactured or cladded, we closely examine the conditions that favor the formation of such features. It appears that a complex interplay between the recoil pressure and the Marangoni force inside the melt pool determines the interface morphology, which is also depends on D_m / W_m, as discussed below.

When the melt pool is shallow and wide (D_m / W_m < 0.25), the recoil pressure acts between the keyhole and the cross-section C-C and pushes the molten IN718 in the direction opposite to the scan direction. The parallel Marangoni force acts between the cross-sections C-C and D-D [Fig. 6(a)]. On the perpendicular cross-section B-B located near the keyhole, the melt pool is driven by the perpendicular Marangoni force that acts parallel to it, causing the melt pool to experience convective movements that are clockwise and counter-clockwise on the right and left sides of the vertical center line of the melt pool, respectively [Fig. 6(b)]. On the perpendicular cross-section C-C that is slightly further away from the keyhole, the cooling of the melt pool surface leads to an opposite trend of perpendicular Marangoni force on the cross-section B-B. As such, the melt pool flow causes counter-clockwise and clockwise convective motions on the right- and left-hand side edges of the vertical center line, respectively [Fig. 6(c)]. Far from the keyhole on cross-section D-D, the melt pool is in the solidification range [Fig. 6(d)]. Due to the marginal penetration of the melt pool into the substrate, insufficient dissimilar materials are available for the formation of markedly interpenetrating interface between IN718 and 316L (Movie S3); a marginal penetration of IN718 into 316L results in a staggered but overlapping layer morphology that is akin to those seen in general "fish scale" [Fig. 5(a) and Fig. 6(e)].

Upon an increase in the keyhole depth to medium-deep and narrow (0.25 ≤ D_m / W_m < 0.55), part of the recoil pressure is used for maintaining the shape of the keyhole while the other part pushes the molten IN718 in the direction opposite to the scan direction. The recoil pressure that acts between the keyhole and cross-section B-B and the parallel Marangoni force that acts between the cross-sections B-B and D-D [Fig. 7(a)] move down the IN718 melt at a distance approximately equal to D_m (Movie S6). The movement trend and mechanism of the melt pool in the regions between the cross-sections B-B and D-D are the same as those seen in the case of the shallow melt pool depth (D_m / W_m < 0.25, see Figs. 6(b)-(d)). However, the perpendicular Marangoni force direction trend is more pronounced at this medium-deep and narrow melt pool (0.25 ≤ D_m / W_m <

0.55), see Fig. 7(b)-(d). The solidification interface between the two alloys adapts a staggered and independent "fish scale" morphology [Fig. 5(b) and Fig. 7(e)].

When the melt pool is deep and narrow (D_m / W_m $\geq$ 0.55), the recoil pressure, which mainly acts to maintain a deep but unstable keyhole, and the parallel Marangoni force that acts between the cross-sections B-B and D-D [Fig. 8(a)] push the molten IN718 deep into 316L. The Marangoni force and recoil pressure led to melt insertion on both sides of the melt pool boundary to form two IN718 planes. In the end, the interface between the two alloys forms an independent but irregular "strip" morphology [Fig. 8(e)].

For illustrative purposes, melt pool boundary angle α and β for two different (and orthogonal) cross-sections of A-A and B-B are depicted in Fig. 7(a) and (d) . Fig. S2 contains detailed description of α and β in shallow (I), intermediate (II) and deep (III) melt pools. In these illustrations, $D_{m,\ I}$, $D_{m,\ II}$ and $D_{m,\ III}$ refer to the depth of the melt pools Ⅰ, Ⅱ and Ⅲ respectively. α is the characteristic angle between the melt pool boundary and the plane perpendicular to the build direction, located on the parallel cross-section A-A [Fig. 7(a)]. L1 is the intersection line between the plane perpendicular to the build direction and the cross-section A-A. L2 is on the cross-section A-A, and its beginning point is the intersection between the melt pool boundary and the lowest end of the fish scale, and its ending point is on the melt pool boundary. The length of L2 is D_m / 2. In other words, α is the angle between L1 and L2. β is the characteristic angle between the melt pool boundary and the plane perpendicular to the build direction, located on the perpendicular cross-section B-B [Fig. 7(d)]. L3 is the intersection line between the plane perpendicular to the build direction and the cross-section B-B. L4 is on the cross-section B-B, and its beginning point is the intersection between the melt pool boundary and the upper surface of the substrate, and the ending point is on the melt pool boundary. The length of L4 is D_m / 2 while β is the angle between L3 and L4. The values of α and β are dictated by the Marangoni forces that act parallel and perpendicular to the melt pool cross-section, respectively, and hence move it upward [Figs. 7(a) and S2(a), and movies S3 and S6] or downward [Figs. 7(d) and S2(b)], respectively, along the melt pool boundary.

Variations of α (obtained from simulation) and β (both experimental and simulation values) with D_m / W_m are plotted in Fig. 9. (The values of α from experiments could not be obtained due to the difficulty in estimating them from the cross-sectioned single-track scans.) As seen, α varies between 0° and 50° whereas β between 0° and 80°. Even though multiple L-V combinations were

used, well-defined trends in both α and β emerge. With an increase in D_m / W_m, both α and β decrease. An agreement between the experimental and simulated variations in β with D_m / W_m confirms the fidelity of the simulations performed in this work. When D_m / W_m < 0.55, α increase sharply, and when D_m / W_m ≥ 0.55, α slowly increases to 80°. When D_m / W_m < 0.55, β increase linearly, and when D_m / W_m ≥ 0.55, β slowly increases to 50°. The correlation of α and β and D_m / W_m on the interface strength will be discussed in Section 5.1.

4.2 Interface compositional distribution and microstructures

EDS was conducted to map the elemental distributions on cross-sections A-A and E-E. For the sake of brevity, the spatial distributions of each alloy in the EDS maps displayed in Figs. 10 - 11 and S3 are identified by their principal elements: Ni for IN718 and Fe for 316L. The influence of different scan strategies on the distribution of the two alloys can be gauged through these maps, with IN718 having the characteristic curved strips and swirls in 2D, which is a prerequisite for the formation of an interpenetrating interface in 3D. Both the simulation and experiment results in 2D showed similar component distribution characteristics of IN718, which further confirmed the validity of the simulation.

When the interdiffusion between the two alloys is extensive, such as that seen in the cross-section of the single track with D_m / W_m = 1.16 [Fig. 11(a)], the compositional contrast at the interface is no longer obvious. Keeping this in view, the degree of interdiffusion between the two alloys is assessed using the 'degree of alloying (DoA)' that is defined using the content of alloying elements, serving as an index to evaluate the influence of the interface morphology on the material's microstructure. The two alloys, 316L and IN718 contain 65.5 and 16.9 wt% of Fe, respectively. The difference in the Fe content is 48.6 wt%. EDS was then utilized to map the proportion of Fe, C_{Fe} on the single melt pool's cross-section [Fig. S4(a)], based on which DoA in each scanned pixel can be obtained [Fig. S4(b)], assuming a piecewise linear relationship with C_{Fe}:

$$\mathrm{DoA} = \begin{cases} C_{\mathrm{Fe}}/24.3 - 0.695 & \text{for } 16.9 \le C_{\mathrm{Fe}} \le 41.2 \\ C_{\mathrm{Fe}}/24.3 + 2.695 & \text{for } 41.2 \le C_{\mathrm{Fe}} \le 65.5 \end{cases} . \tag{11}$$

According to the above scheme, a DoA value of 1 represents complete interdiffusion between the two alloys in which C_{Fe} is 41.2 wt% whereas a value of 0 represents no interdiffusion in which

C_{Fe} is either 16.9 or 65.5 wt%, representing pure 316L or pure In718, respectively. For visual representation of DOA across the solidified interface with different *L* and *V*, its values are binned into four levels [Table. 1] and are represented in Fig. S5.

Table. 1. DoA level of two alloys and their corresponding range.

DoA level	Level 1	Level 2	Level 3	Level 4
DoA	0 ≤ DoA < 0.25	0.25 < DoA ≤ 0.50	0.50 < DoA ≤ 0.75	0.75 < DoA ≤ 1.00
Interdiffusion state	Limited	General	Majority	Near-complete

The microstructure of the interface was investigated using EBSD; see Figs. 10 and 11. In the parallel cross-section A-A, curved grains that closely follow the fish scale interface morphology (Fig. 10) could be noted, which is in marked contrast with the columnar grains that typically form during LPBF produced 316L processed under similar conditions [49, 50]. Macro-scale segregation of the elements during solidification enables preferential grain growth along compositionally similar regions to minimize free energy [51, 52, 53]. For $0.25 \leq D_m / W_m < 0.55$, curved grains are also observed on the cross-section E-E (Fig. 11). For $D_m / W_m \geq 0.55$, the shape of the grains observed on the cross-section E-E appear to be columnar. The specific reasons are discussed in detail in Section 5.2.

5. DISCUSSION

5.1 Interpenetrating interface formation

The formation of an interpenetrating interface during LPBF of multi-materials was observed and reported in couple of prior studies [15,54]. However, a detailed description of the interface structure was not attempted in those studies, which is possibly due to the usage of metallographic observations, made in 2D that would not allow the capture of the curved nature of the interfaces in 3D. The simulations performed in the present work allow for capturing the evolution of interface geometry in the 3D space and hence enable complete visualization and quantification of the interface characteristics. Although the observations made here pertain to the specific material combination used in this paper, their implications can be adapted to other combinations due to the common nature of melt pool formation and future experimental parametric studies.

One of the biggest assumptions in our simulation is the lack of chemical diffusion. To justify the applicability of our model in this study, we need to first owe up to the shortcoming of not being able to predict the thickness of the diffusion layer. Aside from that, the description of melt-flow characteristics and interface shape based on our simulation remains sufficiently accurate, as observed from the experimental results. This is in fact not surprising as the model did suitably consider the effect of compositional gradient on thermal history, which includes the change in solidus and liquidus temperature due to compositional differences at the interface region. Essentially, the temperature gradient as influenced by the dissimilar alloys was considered, which then affects the different driving forces for heat and mass transfer such as Marangoni force, surface force and recoil force. The good agreement between simulation and experiment could also be due to the inherently fast cooling cycle of LPBF that limits the extent of interdiffusion.

That being said, the simulated results will surely be more accurate if interdiffusion was to be considered, which the change in liquidus and solidus temperatures across the two dissimilar alloys will be more gradual as compared to that in our model. Consequently, there is a limit in our model to accurately describe fluid phenomena at a length scale smaller than the diffusion length. Fortunately, with the agreement of interface shape between the experiment and model, the melt pool dimensions which are of a larger length scale have a good match too, at least within the parameter window we had investigated.

The observation of the melt pool flow during LPBF of dissimilar alloys suggests that the *L*-*V* combination strongly influences the melt pool characteristics (such as α, β, and D_m / W_m) [55,56]. This, in turn, affects the spatial profile of the interface that forms [57]. For instance, the outer boundaries of the "fish scale" interface conform to the melt pool boundaries, Fig. 7. The complex interplay between the Marangoni forces can be simplified by treating them as two separate forces that operate on the two orthogonal planes. The combined effects of these forces result in the 3D “fish scale” morphology, as seen in Fig. S6.

One of the melt pool characteristics that correlates well with the type of interface is the D_m / W_m ratio. As it increases, the interface evolves from an overlapping and staggered "fish scale" interface with a marginal penetration, to an independent and staggered "fish scale" morphology, and finally adapts an irregular “strip” morphology [Figs. 6(e) – 8(e)]. These morphological changes are caused by the transition of melt pool forming mechanism from conduction mode to severe keyhole mode, which is typically seen with increasing *L* or decreasing *V*. In the conduction

dominated melting, the melt pool solidifies quickly before IN718 has a chance to sufficiently penetrate the 316L substrate, hence limiting the amount of 316L available for independent "fish scale" interface formation. Nevertheless, Marangoni force still dominates the induction of fluid flow in the melt pool. Hence, "fish scale" still forms but in an overlapping fashion (see Fig. 6). A transition from conduction to keyhole mode melt pool formation is typically accompanied by stronger Marangoni forces and recoil pressure as well as prolonged melt pool solidification time. In such a scenario, the recoil pressure enhances the Marangoni force induced vortex, and the effective travel distance of the molten alloy into the substrate increases, which leads to swirling that further enhances the penetration depth (see Fig. 7). As the keyhole melting intensifies, the effect of recoil pressure manifests and lead to deep but unstable penetration of IN718 forming irregular strips (see Fig. 8). It is interesting to note here that prior multi-material simulation [20] does not report such observations on the evolution of interface morphology and the "fish scale" formation, possibly because of the low laser absorptivity (~0.03) that leads to only the conduction mode of melting.

An important interface characteristic that varies with the above mentioned evolution of the interface morphology with the D_m / W_m ratio is the interface area (as observed from Figs. 6 to 8 and movies S1 and S4). The interface area is enhanced by the increased swirling and thereby thinning of IN718 prior to solidification, or by the deeper penetration of IN718 due to strong recoil pressure. Such swirling and inter-penetration could enhance the adhesive strength of the interface and may reduce the thermal stress concentration caused by the difference in coefficient of thermal expansion [58]. Keeping this in view, we defined the normalized interfacial area (NIA) to quantitatively evaluate the contribution of laser melting under different process parameters to the growth of the interface area, as:

$$\mathrm{NIA} = \frac{A_\mathrm{m}}{A_\mathrm{mi}} \times 100\% = \frac{A_\mathrm{m}}{W_\mathrm{m} L_\mathrm{m}} \ , \tag{12}$$

where A_mi is the interface area without the effect of laser melting, i.e., a perfectly flat and smooth entity, A_m is the actual interface area, and L_m and W_m are the simulated melt pool length and width, respectively, as illustrated in Fig. 2. The NIA can be treated as a parameter that captures the increment in the interfacial area due to various forces over an unit area of melt pool formation. Essentially, NIA is an intensive parameter and can be suitably applied for the case of single layer scan with multiple single tracks. The normalization of A_m with A_mi enables the cross comparison between the effect of different laser parameters on interface area increment.

The variation of NIA with D_m / W_m is shown in Fig. 12(a). The D_m / W_m axis in Fig. 12(a) is segmented into 3 regions to indicate the D_m / W_m associated with general, "fish scale" and "strip" morphologies of the interface. As D_m / W_m increases, NIA increases with diminished return.

In the overlapping "fish scale" interface region (D_m / W_m < 0.25), NIA increases sharply with D_m / W_m. This region is associated with conduction dominated melting and the penetration of IN718 into the 316L substrate is marginal. As the penetration depth increases, more 316L will take part in interface formation. At the same time, an increase in the Marangoni forces will enhance the swirling and thinning of IN718 in between 316L. The combined effect of these two factors results in a sharp increase of NIA.

In the independent "fish scale" interface region (0.25 ≤ D_m / W_m < 0.55), significant keyhole melting starts to take part and the effect of recoil pressure manifests. The strong recoil pressure along with enhanced Marangoni forces further intensifies the swirling and thinning of the IN718, subsequently leading to NIA increment. However, the rate of NIA increment diminishes as compared to that in the general interface region. The diminished return is mainly due to the already sufficient 316L in the melt pool for interface formation.

In the "strip" interface region, the NIA plateaus with negligible increment when D_m / W_m increases (D_m / W_m ≥ 0.55). The transition to severe keyhole formation leads to intensive recoil pressure and Marangoni forces. However, the swirling of IN718 in 316L does not lead to further thinning of IN718 due to limitation imposed by surface tension, hence limiting the NIA increment.

A plot of NIA against α and β is shown in Fig. 12(b). As α and β are closely related to D_m / W_m, an increase in them also leads to increase in NIA. As seen, NIA rises sharply with α and plateaus after a α of about 18 °. Meanwhile, NIA rises sharply between β of 0 and 30 °, and then increases in a shallow fashion at higher β.

Up to this point, it seems that an increase in D_m / W_m, α and β will always be beneficial in increasing the NIA. However, NIA that is too large might not be the most ideal interface morphology between dissimilar alloys, as it can be limited by factors such as the degree of alloying (DoA). This discussed in the subsequent sections.

5.2 The degree of alloying of dissimilar alloys and curved grain formation

Although significant interdiffusion between 316L and IN718 could be observed for D_m / W_m ≥ 0.55 [Fig. 11(a) and within the parameter window 1 in Fig. S3], the "diluted" IN718 continues

to exhibit an inter-penetrating interface morphology. This observation reinforces the simulation's ability to describe the general distribution of IN718 relatively accurately, even though diffusion was not taken into account in the model used for it. It is found that when D_m / W_m $\geq$ 0.55, the recoil pressure and Marangoni force cause extensive inter-mixing of the alloys within the melt pool [Fig. 8]. About 7.6 vol% of the solidified solid solution is within the first level DoA , while the third and fourth level DoA are between 31.2 and 45.7 vol% [Figs. S5 and 11(a)]. This result shows that these two alloys exhibit a strong propensity for inter-diffusion. For D_m / W_m < 0.55 [Figs. 11(b) - (d) and outside the parameter window 1 in Fig. S3], the inter-mixing within the melt pool is not as pronounced, and strong compositional contrast can be observed in the experimental results. More than 16.2 vol% of the frozen solid solution is within the first level DoA, indicating strong macro-segregation of IN718 and 316L. The third and fourth level DoA are between 10.8 and 31.1 vol%, indicating that the degree of interdiffusion between the two alloys is limited [Fig. S5]. For L = 200 W and V = 1500 mm/s, both the first and second level DoA reache 30 vol% [Fig. S5], and the Ni-rich curved grains largely retain their original composition of IN718.

When D_m / W_m $\geq$ 0.55 [Fig. 11(a) and within the parameter window 1 in Fig. S3], severe convection within the melt pool leads to farther diffusion of IN718. The first and fourth levels of DoA for such a melt pool are < 7.6 and > 31.2 vol%, respectively [Fig. S5], which indicate strong interdiffusion of the two alloys. The absence of a sharp compositional transition in such a scenario results in the absence of curved grains in the solidified microstructure. Instead, the grain morphology is akin to that produced in LPBF of 316L on 316L, with most of the grains being perpendicular to the melt pool boundary [50]. In dissimilar alloy systems with high DoA, in contrast, the macroscopic thermal gradient dominates the grain growth [59, 60].

For 0.25 $\leq$ D_m / W_m < 0.55 [Fig. 11(b) and (c), and within the parameter window 2 in Fig. S3]), the distance that molten IN718 flows convectively is approximately equal to D_m. An increase in first level DoA's proportion and a commensurate decrease in the fourth level DoA leads to a uniform distribution in the chemical constituents [Fig. S5], resulting in insufficient DoA between the alloys, which leads to distinct physical and chemical properties on either of the "fish scales" [the inner side of the fish scale interface is mainly IN718 whereas the outer side is mainly 316L, see Fig. S4(a)]. As expected, the interdiffusion of the two alloys at the "fish scale" interface is the greatest [Fig. S4(b)], while the composition in the middle of "fish scale" largely retains that of IN718 [Fig. S4(a)]. Consequently, the alloy composition dominates the grain growth, resulting in

curved grains in order to minimize the free energy. In the extreme case, the curved compositional profiles can induce curved grains with a curvature close to 180° (L = 200 W & V = 1200 or 1500 mm/s, and L = 300 W & V = 1200 mm/s in Figs. S3 and S5). The thickness of IN718 or 316L within the "fish scale" ranges between 5 and 25 μm, which is approximately equal to the typical grain thickness produced via LPBF for such a material (In general, the grain thickness produced by LPBF 316L ranges between 10 and 30 μm) [12 ,19 , 50]. For D_m / W_m < 0.25 [Fig. 11(d) and outside the parameter window 1 and 2 in Fig. S3], molten IN718 has a short convective flow distance. The first and fourth level DoA increase and decrease, respectively, to 59.5 and 10.8 vol% [L = 100 W, V = 1500 mm/s in Fig. S5], indicating insignificant interdiffusion between the two alloys. Though a sharp chemical transition exists, neither IN718 or 316L form a thin "fish scale". Instead, (possibly) polycrystalline globules with an equivalent diameter > 45 μm, which is larger than the grain size observed in a typical LPBF manufactured 316L, forms within a region of self-similar composition (L = 100 W & V = 1200, and L = 300 W & V = 2100 mm/s in Fig. S3). Thus, both the temperature gradient and composition dominate the grain growth mechanism in this case, resulting in columnar grains with occasional discontinuity near the alloy boundary at low DoA.

When 0.25 ≤ D_m / W_m < 0.55, curved grains were observed on both parallel and perpendicular cross-sections of the track, confirming the existence of curved fish scale formation in 3D. This observation indicates that the grain shape and size are affected by the distribution of alloys at the interface (Figs. 11 and S5). Generally, curved grains are typically accompanied by thin "fish scale" and moderate inter-diffusion (medium DoA).

5.3 LPBF process parameter optimization

Based on the discussion above, it is clear that the parameter optimization for interface is not a straightforward process, and various tradeoffs need to be considered. An increment in NIA signifies better inter-penetration between the dissimilar alloys, which can lead to higher interfacial strength due to better stress transfer between them. However, when NIA exceeds 1050 (when D_m / W_m ≥ 0.55), the high DoA could lead to dilution of both the alloys, which effectively removes the multi-alloy interface, akin to that of a drop of ink added to a cup of water that is stirred. It should be noted that the formation of curved grains is observed under medium DoA conditions (675 <NIA< 1050 in the case of 718/316L interface and the melt pool parameters of 0.25 ≤ D_m / W_m < 0.55, 8° < α < 18° and 30 ° < β < 60 °).

The methodology for such optimum process window identification should always involve the exploration of laser parameters that cover both extremes of interface evolution, from conduction melting to severe keyhole melting. The interface evolution as observed in this study would be applicable any melting process that has moving focused energy source. Therefore, it should be possible to observe similar phenomena in the directed energy deposition process as well. Needless to say, extensive simulation and experimental work needs to be conducted to achieve a full size multi-material component with a strong interface. A key aspect for realizing this would be to impart minimal changes to the 'fish scale' interfaces during the subsequent layer deposition, which can be achieved by switching over to the conduction mode of melting.

6. CONCLUSIONS

Simulations and experiments of the single-track laser melting of IN718 powder onto 316L substrate have shown that the formation of "fish scale" interface between the two dissimilar alloys can occur under certain combinations of process parameters. A detailed analysis on the melt pool flow characteristics has shown that such an interface as a consequence of the combined action of recoil pressure, Marangoni forces, surface tension and melt pool shape, which are exemplified by parameters α, β and D_m / W_m. When the melt pool is shallow and wide (D_m / W_m < 0.25), the solidification interface between the two alloys presents a staggered but overlapping general "fish scale" morphology and the normalized interfacial area (NIA) is less than 675; for the medium-deep and narrow melt pool ($0.25 \leq D_m$ / $W_m < 0.55$), the solidification interface between the two alloys adapts a staggered and independent "fish scale" morphology and the NIA is between 675 and 1050. Finally, when the melt pool is deep and narrow (D_m / $W_m \geq 0.55$), the solidification interface between the two alloys has an independent but irregular "strip" morphology and the NIA is greater than 1050.

The LPBF process parameters (L and V) dictate the "fish scale" interface shape (melt pool shape), while the exact shape and size of the "fish scale" has close relation with the degree of alloying (DoA) and the grain morphology. The "fish-scale" shape (related to molten pool shape parameters, $0.25 \leq D_m$ / $W_m < 0.55$, $8° < \alpha < 18°$, $30 ° < \beta < 60 °$) and degree of alloying (Medium DoA) and normalized interfacial area ($675 \leq$ NIA < 1050) between the dissimilar alloys can produce curved grains within a well-defined threshold. The interlocked and entangled curved

grains and alloy composition distributions with fish-scale morphology have the potential to enhance the strength of the interface.

ACKNOWLEDGEMENTS

Funding for this work was provided by A*STAR SERC AME Programmatic Fund for the "Structural Metal Alloys Programme" (A18B1b0061) and Singapore Centre for 3D Printing under the project "Acquisition and reconstruction of 3D CAD models for repair and re-engineering".

References

[1] C. Zhang, F. Chen, Z. F. Huang, M. Y. Jia, G. Y. Chen, Y. Q. Ye, Y. J. Lin, L. Wei, B. Q. Chen, Q. Shen, Additive manufacturing of functionally graded materials: A review, Mater. Sci. Eng. A.764 (2019) 138209, doi: 10.1016/j.msea.2019.138209.

[2] Y. Wen, B. Zhang, R. L. Narayan, P. Wang, X. Song, H. Zhao, X. Qu, Laser powder bed fusion of compositionally graded CoCrMo-Inconel 718, Addit Manuf. 40 (2021) 101926, doi: 10.1016/j.addma.2021.101926.

[3] C. Guo, W. Ge, F. Lin, Dual-material electron beam selective melting: hardware development and validation studies, Engineering. 1(1) (2015) 124-130, doi: 10.15302/J-ENG-2015013.

[4] J. Walker, J. Middendorf, C. Lesko, J. Gockel, Multi-material laser powder bed fusion additive manufacturing in 3-dimensions, Manuf. Lett. (2021) doi: 10.1016/j.mfglet.2021.07.011.

[5] R. Wang, D. Gu, C. Chen, D. Dai, C. Ma, H. Zhang, Formation mechanisms of TiB2 tracks on Ti6Al4V alloy during selective laser melting of ceramic-metal multi-material, Powder Technol. 367 (2020) 597-607, doi: 10.1016/j.powtec.2020.04.027.

[6] A. G. Demir, B. Previtali, Multi-material selective laser melting of Fe/Al-12Si components, Manuf. Lett. 11 (2017) 8-11. doi: 10.1016/j.mfglet.2017.01.002.

[7] W. Zhai, P. Wang, F. L. Ng, W. Zhou, S. M. L. Nai, J. Wei, Hybrid manufacturing of γ-TiAl and Ti–6Al–4V bimetal component with enhanced strength using electron beam melting, Compos. B: Eng. 207 (2021) 108587. doi: 10.1016/j.compositesb.2020.108587.

[8] W. Meng, X. H. Yin, Z. Wang, J. F. Fang, L. J. Guo, Q. S. Ma, B. Cui, Additive manufacturing of a functionally graded material from Inconel625 to Ti6Al4V by laser synchronous preheating, J Mater Process Technol. 275 (2020) 116368, doi: 10.1016/j.jmatprotec.2019.116368.

[9] L. D. Bobbio, R. Otis, J. P. Borgonia, R. P. Dillon, A. A. Shapiro, Z. -K. Liu, A. M. Beese, Additive manufacturing of a functionally graded material from Ti-6Al-4V to Invar: Experimental characterization and thermodynamic calculations, Acta Mater. 127 (2017) 133-142, doi: 10.1016/j.actamat.2016.12.070.

[10] P. Kumar, U. Ramamurty, Microstructural optimization through heat treatment for enhancing the fracture toughness and fatigue crack growth resistance of selective laser melted Ti6Al4V alloy, Acta Mater. 169 (2019) 45-59, doi: 10.1016/j.actamat.2019.03.003.

[11] C. F. Tey, X. Tan, S. L. Sing, W. Y. Yeong, Additive manufacturing of multiple materials by selective laser melting: Ti-alloy to stainless steel via a Cu-alloy interlayer, Addit Manuf. 31 (2020) 100970, doi: 10.1016/j.addma.2019.100970.

[12] A. Reichardt, R. P. Dillon, J. P. Borgonia, A. A. Shapiro, B. W. McEnerney, T. Momose, P. Hosemann, Development and characterization of Ti-6Al-4V to 304L stainless steel gradient components fabricated with laser deposition additive manufacturing, Mater. Des. 104 (2016) 404-413, doi: 10.1016/j.matdes.2016.05.016.

[13] J. Shinjo, C. Panwisawas, Digital Materials Design by Thermal-Fluid Science for Multi-Metal Additive Manufacturing, Acta Mater. 210 (2021) 116825. doi: 10.1016/j.actamat.2021.116825.

[14] L. Yan, Y. Chen, F. Liou, Additive manufacturing of functionally graded metallic materials using laser metal deposition, Acta Mater. 127 (2020) 100901, doi: 10.1016/j.addma.2019.100901.

[15] J. Koopmann, J. Voigt, T. Niendorf, Additive Manufacturing of a Steel-Ceramic Multi-Material by Selective Laser Melting, Metall. Mater. Trans. 50 (2019) 1042-1051, doi: 10.1007/s11663-019-01523-1.

[16] R. Shi, S. A. Khairallah, T. T. Roehling, T. W. Heo, J. T. McKeown, M. J. Matthews, Microstructural control in metal laser powder bed fusion additive manufacturing using laser beam shaping strategy, Acta Mater. 184 (2020) 284-305, doi: 10.1016/j.actamat.2019.11.053.

[17] Y. Zhang, A. Bandyopadhyay, Direct fabrication of compositionally graded Ti-Al2O3 multi-material structures using Laser Engineered Net Shaping, Addit Manuf. 21 (2018) 104-111, doi: 10.1016/j.addma.2018.03.001.

[18] M. Naebe, K. Shirvanimoghaddam, Functionally graded materials: A review of fabrication and properties, Appl. Mater. Today. 5 (2016) 223-245, doi: 10.1016/j.apmt.2016.10.001.

[19] S. M. Yusuf, X. Zhao, S. Yang, N. Gao, Interfacial characterisation of multi-material 316L stainless steel/Inconel 718 fabricated by laser powder bed fusion, Mater. Lett. 284 (2020) 128928, doi: 10.1016/j.matlet.2020.128928.

[20] H. Gu, C. Wei, L. Li, Q. Q. Han, R. Setchi, M. Ryan, Q. Li, Multi-physics modelling of melt pool development and track formation in multi-track, multi-layer and multi-material selective laser melting, Int. J. Heat Mass Transf. 151 (2020) 119458, doi: 10.1016/j.ijheatmasstransfer.2020.119458.

[21] Q. Guo, C. Zhao, L. I. Escano, Z. Young, L. Xiong, K. Fezzaa, L. Chen, Transient dynamics of powder spattering in laser powder bed fusion additive manufacturing process revealed by in-situ high-speed high-energy x-ray imaging, Acta Mater. 151 (2018) 169-180, doi: 10.1016/j.actamat.2018.03.036.

[22] B. E. Kelly, I. Bhattacharya, H. Heidari, M. Shusteff, C. M. Spadaccini, H. K. Taylor, Volumetric additive manufacturing via tomographic reconstruction, Science 363(6431) (2019) 1075-1079, doi: 10.1126/science.aau7114.

[23] B. Onuike, A. Bandyopadhyay, Additive manufacturing of Inconel 718-Ti6Al4V bimetallic structures, Addit Manuf. 22 (2018) 844-851, doi: 10.1016/j.addma.2018.06.025.

[24] A. A. Martin, N. P. Calta, S. A. Khairallah, J. Wang, P. J. Depond, A. Y. Fong, C. J. Tassone, Dynamics of pore formation during laser powder bed fusion additive manufacturing, Nat. Commun. 10(1) (2019) 1-10, doi: 10.1038/s41467-019-10009-2.

[25] W. Li, F. Liou, J. Newkirk, K. M. B. Taminger, W. J. Seufzer, Investigation on Ti6Al4V-V-Cr-Fe-SS316 multi-layers metallic structure fabricated by laser 3D printing, Sci. Rep. 7(1) (2017) 1-14, doi: 10.1038/s41598-017-08580-z.

[26] Z. H. Liu, D. Q. Zhang, S. L. Sing, C. K. Chua, L. E. Loh, Interfacial characterization of SLM parts in multi-material processing: Metallurgical diffusion between 316L stainless steel and C18400 copper alloy, Mater Charact. 94 (2014) 116-125, doi: 10.1016/j.matchar.2014.05.001.

[27] R. Koike, I. Unotoro, Y. Kakinuma, T. Aoyama, Y. Oda, T. Kuriya, M. Fujishima, Evaluation for mechanical characteristics of Inconel625-SUS316L joint produced with direct energy deposition, Procedia Manuf. 14 (2017) 105-110, doi: 10.1016/j.promfg.2017.11.012.

[28] L. D. Bobbio, B. Bocklund, R. Otis, J. P. Borgonia, R. P. Dillon, A. A. Shapiro, A. M. Beese, Experimental analysis and thermodynamic calculations of an additively manufactured functionally graded material of V to Invar 36, J. Mater. Res. 33(11) 1642, doi: 10.1557/jmr.2018.92.

[29] C. Tan, K. Zhou, T. Kuang, Selective laser melting of tungsten-copper functionally graded material, Mater. Lett. 237 (2019) 328-331, doi: 10.1016/j.matlet.2018.11.127.

[30] Y. H. Chueh, X. Zhang, J. C. R. Ke, Q. Li, C. Wei, L. Lin, Additive manufacturing of hybrid metal/polymer objects via multiple-material laser powder bed fusion, Addit Manuf. 36 (2020) 101465, doi: 10.1016/j.addma.2020.101465.

[31] Y. T. Pei, J. T. M. De Hosson, Functionally graded materials produced by laser cladding, Acta materialia 48(10) (2000) 2617-2624, doi: 10.1016/S1359-6454(00)00065-3.

[32] B. E. Carroll, R. A. Otis, J. P. Borgonia, J. O. Suh, R. P. Dillon, A. A. Shapiro, A. M. Beese, Functionally graded material of 304L stainless steel and inconel 625 fabricated by directed energy deposition: Characterization and thermodynamic modeling, Acta Mater. 108 (2016) 46-54, doi: 10.1016/j.actamat.2016.02.019.

[33] C. Wei, H. Gu, Q. Li, Z. Sun, Y. H. Chueh, Z. Liu, L. Li,. Understanding of process and material behaviours in additive manufacturing of Invar36/Cu10Sn multiple material components via laser-based powder bed fusion, Addit Manuf. 37 (2021), 101683, doi: 10.1016/j.addma.2020.101683.

[34] C. Wei, L. Li, X. Zhang, Y. H. Chueh, 3D printing of multiple metallic materials via modified selective laser melting, CIRP Annals 67(1) (2018) 245-248, doi: 10.1016/j.cirp.2018.04.096.

[35] A. A. Ward, Z. C. Cordero, Junction growth and interdiffusion during ultrasonic additive manufacturing of multi-material laminates, Scr. Mater. 177 (2020) 101-105, doi: 10.1115/1.4043983.

[36] C. C. Tseng, C. J. Li, Numerical investigation of interfacial dynamics for the melt pool of Ti-6Al-4V powders under a selective laser, Int. J. Heat Mass Transf. 134 (2019) 906-919, doi: 10.1016/j.ijheatmasstransfer.2019.01.030.

[37] M. Bayat, S. Mohanty, J. H. Hattel, A systematic investigation of the effects of process parameters on heat and fluid flow and metallurgical conditions during laser-based powder bed fusion of Ti6Al4V alloy, Int. J. Heat Mass Transf. 139 (2019) 213-230, doi: 10.1016/j.ijheatmasstransfer.2019.05.017.

[38] K. Q. Le, C. Tang, C. H. Wong, On the study of keyhole-mode melting in selective laser melting process, Int J Therm Sci. 145 (2019) 105992, doi: 10.1016/j.ijthermalsci.2019.105992.

[39] H. Gu, L. Li, Computational fluid dynamic simulation of gravity and pressure effects in laser metal deposition for potential additive manufacturing in space, Int. J. Heat Mass Transf. 140 (2019) 51-65, doi: 10.1016/j.ijheatmasstransfer.2019.05.081.

[40] H. Chen, W. Yan, Spattering and denudation in laser powder bed fusion process: Multiphase flow modelling, Acta Mater. 196 (2020) 154-167, doi: 10.1016/j.actamat.2020.06.033.

[41] Z. Sun, Y.-H. Chueh, L. Li, Multiphase mesoscopic simulation of multiple and functionally gradient materials laser powder bed fusion additive manufacturing processes, Addit Manuf. 35 (2020) 101448, doi: 10.1016/j.addma.2020.101448.

[42] V. R. Voller, A. D. Brent, C. Prakash, The modelling of heat, mass and solute transport in solidification systems, Int. J. Heat Mass Transf. 32(9) (1989) 1719-1731, doi: 10.1016/0017-9310(89)90054-9.

[43] C. Tang, K. Q. Le, C. H. Wong, Physics of humping formation in laser powder bed fusion, Int. J. Heat Mass Transf. 149 (2020) 119172, doi: 10.1016/j.ijheatmasstransfer.2019.119172.

[44] S. A. Khairallah, A. T. Anderson, A. Rubenchik, W. E. King, Laser powder-bed fusion additive manufacturing: Physics of complex melt flow and formation mechanisms of pores, spatter, and denudation zones, Acta Mater. 108 (2016) 36-45, doi: 10.1016/j.actamat.2016.02.014.

[45] K. C. Mills, Recommended values of thermophysical properties for selected commercial alloys. Woodhead Publishing, England, 2002.

[46] M. J. McNallan, T. Debroy, Effect of temperature and composition on surface tension in Fe-Ni-Cr alloys containing sulfur, Metall. Trans. B. 22(4) (1991) 557-560.

[47] S. A. Khairallah, A. A. Martin, J. R. I. Lee, G. Guss, N. P. Calta, J. A. Hammons, M. H. Nielsen, K. Chaput, E. Schwalbach, M. N. Shah, Controlling interdependent meso-nanosecond dynamics and defect generation in metal 3D printing, Science. 368 (2020) 660-665, doi: 10.1126/science.aay7830.

[48] J. Metelkova, Y. Kinds, K. Kempen, C. Formanoir, A. Witvrouw, B. Van Hooreweder, On the influence of laser defocusing in Selective Laser Melting of 316L, Addit. Manuf. 23 (2018) 161169.

[49] A. J. Birnbaum, J. C. Steuben, E. J. Barrick, A. P. Iliopoulos, J. G. Michopoulos, Intrinsic strain aging, Σ3 boundaries, and origins of cellular substructure in additively manufactured 316L, Addit Manuf. 29 (2019) 100784, doi: 10.1016/j.addma.2019.100784.

[50] Y. F. Wang, C. F. Yu, L. L. Xing, K. L. Li, J. H. Chen, W. Liu, J. Ma, Z. J. Shen, Grain structure and texture of the SLM single track, J. Mater. Process. Technol. 281 (2020) 116591, doi: 10.1016/j.jmatprotec.2020.116591.

[51] H. Stünitz, Syndeformational recrystallization - dynamic or compositionally induced?, Contrib. to Mineral. Petrol. 131 (1998) 219-236, doi: 10.1007/s004100050390.

[52] A. Kwiatkowski da Silva, D. Ponge, Z. Peng, G. Inden, Y. Lu, A. Breen, B. Gault, D. Raabe, Phase nucleation through confined spinodal fluctuations at crystal defects evidenced in Fe-Mn alloys, Nat. Commun. 9 (2018) 1137, doi: 10.1038/s41467-018-03591-4.

[53] S.-J. Lee, Y.-K. Lee, Prediction of austenite grain growth during austenitization of low alloy steels, Mater. Des. 29 (2008) 1840-1844, doi: 10.1016/j.matdes.2008.03.009.

[54] F. Hengsbach, P. Koppa, M. J. Holzweissig, M. E. Aydinöz, Al. Taube, K. P. Hoyer, O. Starykov, B. Tonn, T. Niendorf, T. Tröster, M. Schaper. Inline additively manufactured functionally graded multi-materials: microstructural and mechanical characterization of 316L parts with H13 layers, Prog Addit Manuf. 3 (2018) 221-231, doi:10.1007/s40964-018-0044-4.

[55] S. M. H. Hojjatzadeh, N. D. Parab, Q. L. Guo, M. L. Qu, L. H. Xiong, C. Zhao, L. I. Escano, K. Fezzaa, W. Everhart, T. Sun, Direct observation of pore formation mechanisms during LPBF additive manufacturing process and high energy density laser welding, Int. J. Mach. Tools Manuf. 153 (2020) 103555, doi: 10.1016/j.ijmachtools.2020.103555.

[56] M. Bayat, A. Thanki, S. Mohanty, A. Witvrouw, S. Yang, J. Thorborg, N. S. Tiedje, J. H. Hattel, Keyhole-induced porosities in Laser-based Powder Bed Fusion (L-PBF) of Ti6Al4V: High-fidelity modelling and experimental validation, Addit Manuf. 30 (2019) 100835, doi: 10.1016/j.addma.2019.100835.

[57] R. Cunningham, C. Zhao, N. Parab, C. Kantzos, J. Pauza, K. Fezzaa, T. Sun, A. Rollett, Keyhole threshold and morphology in laser melting revealed by ultrahigh-speed x-ray imaging, Science. 363 (2019) 849-852, doi: 10.1126/science.aav4687.

[58] Z. Wang, G. Xian, Effects of thermal expansion coefficients discrepancy on the CFRP and steel bonding, Constr Build Mater. 269 (2021) 121356, doi: 10.1016/j.conbuildmat.2020.121356.

[59] C. Antonione, G. Della Gatta, G. Riontino, G. Venturello, Grain growth and secondary recrystallization in iron, J. Mater. Sci. 8 (1973) 1-10, doi: 10.1007/BF00755577.

[60] M.-S. Pham, B. Dovgyy, P. A. Hooper, C. M. Gourlay, A. Piglione, The role of side-branching in microstructure development in laser powder-bed fusion, Nat. Commun. 11 (2020) 1-12, doi: 10.1038/s41467-020-14453-3.

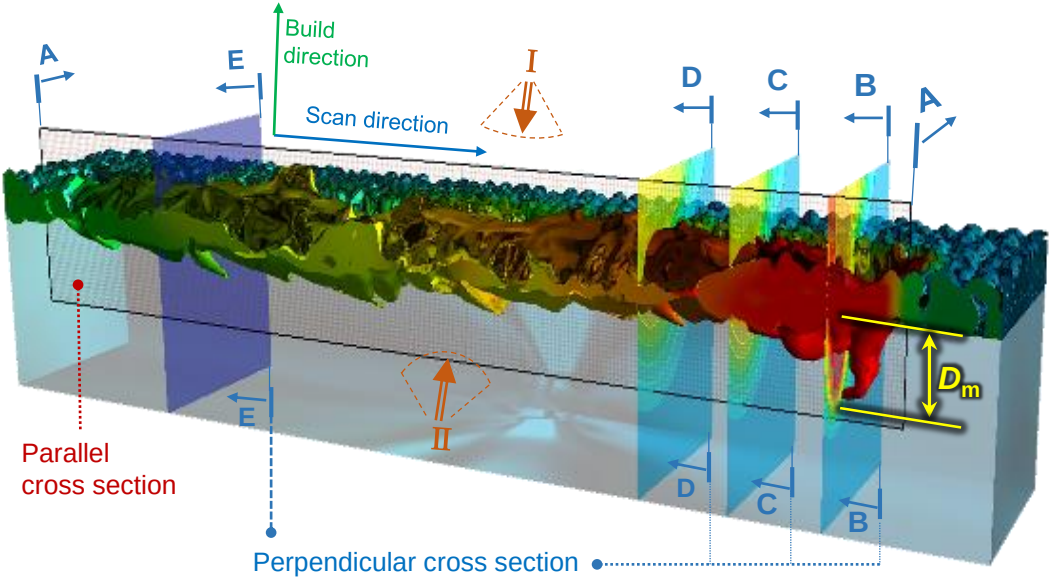

Figure 1. Representative image of a single-track laser scan showing the cross sections used for the extraction of physical parameters and various viewing directions utilized in this study. Cross-section A-A is parallel to the scan and build direction. Cross-sections B-B to E-E are perpendicular to the scan direction while parallel to the build direction. D_m is the distance from the bottom of the melt pool to the top of the substrate.

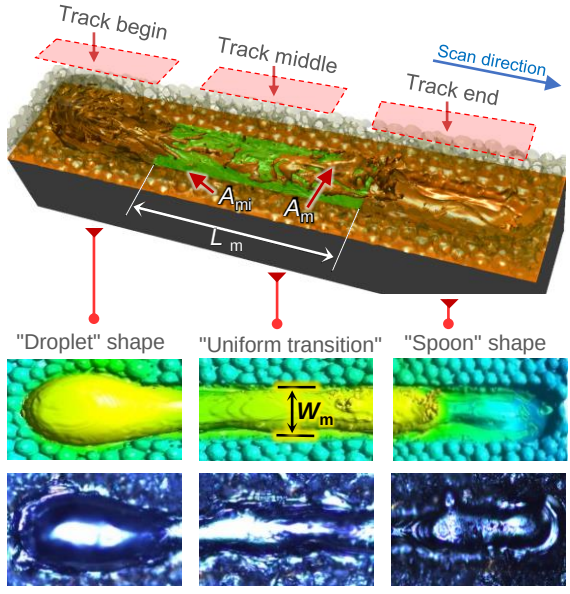

Figure 2. Topography of a single track. While the top picture shows a 3D view of the single track, images in the middle and bottom rows show simulation and experimental results, respectively, (top views) at various locations of the track. W_m is the track width on the top surface of the substrate.

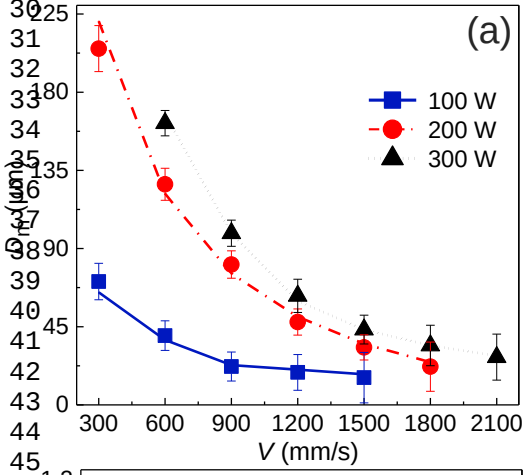

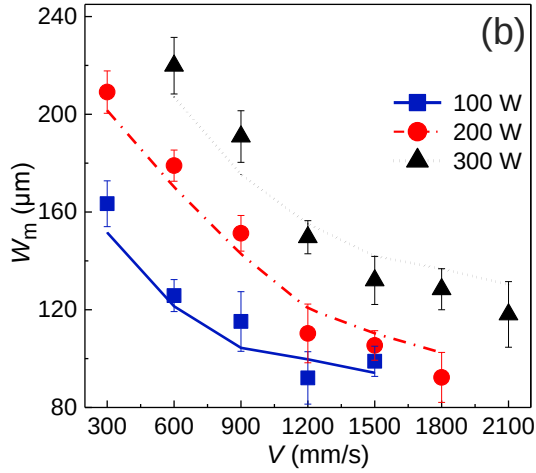

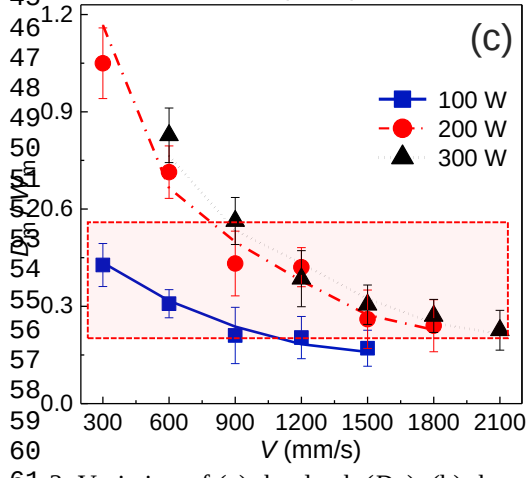

Figure 3. Variation of (a) the depth (D_m), (b) the width (W_m) and (c) the melt pool aspect ratio (D_m / W_m) of the melt pools formed during single track laser melting of IN718 powder on 316L substrate with the scan velocity (V) at three different laser powers (L). Symbols represent the experimental data whereas the lines are simulation results. These data are taken from the cross-section E-E in Figure 1. The shaded region in Figure (c) corresponds to the processing window that produces independent "fish scales", which also exhibits moderate inter-diffusion (medium DoA) that is conducive for the formation of curved grains.

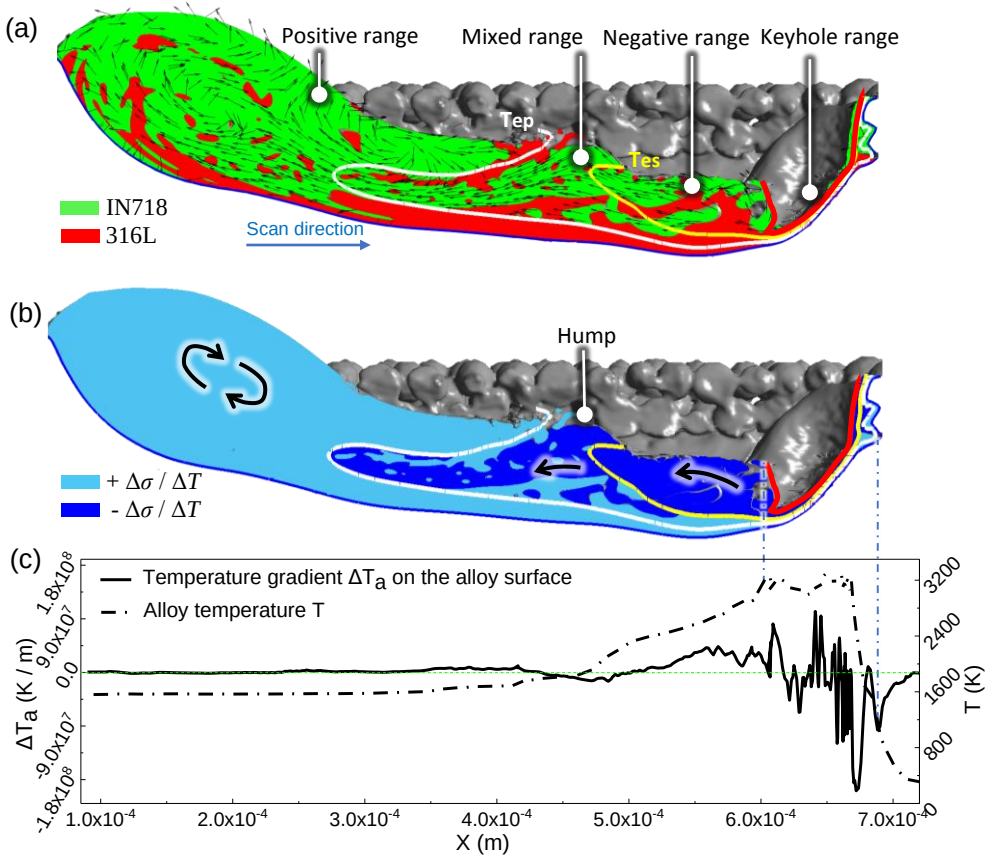

Figure 4. Representative simulation result showing (a) the melt flow, (b) the surface tension gradient and (c) the temperature gradient along the cross-section A-A obtained from the single-track laser scan with L = 200 W and V = 900 mm/s. In Figure (b), the surface tension gradient extracted from the melt pool in Figure (a), Figure (c) is the temperature and temperature gradient on the alloy surface extracted from Figure (b). Color shape code: melt velocity direction - black arrow; melt pool boundary - blue line; T_{ep} isotherm (1801 K) – white line; T_{es} isotherm (2400 K) – yellow line; keyhole boundary – red line; IN718 distribution – green area; 316L distribution – red area; + $\Delta\sigma$ / ΔT – light blue area; -$\Delta\sigma$ / ΔT – dark blue area.

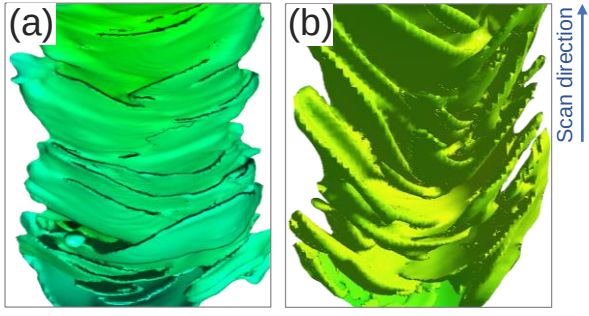

Figure 5. Simulation results showing the “Fish scale” morphology of the interface formed during laser melting of IN718 powder onto SS316L substrate with the scanning parameters (a) L = 200 W, V = 1500 mm/s, representing a typical overlapping and staggered "fish scale" interface and (b) L = 200 W, V = 900 mm/s, representing a typical independent and staggered "fish scale" interface. These images are obtained while viewing the interface from the bottom (viewing angle Ⅱ in Figure 1).

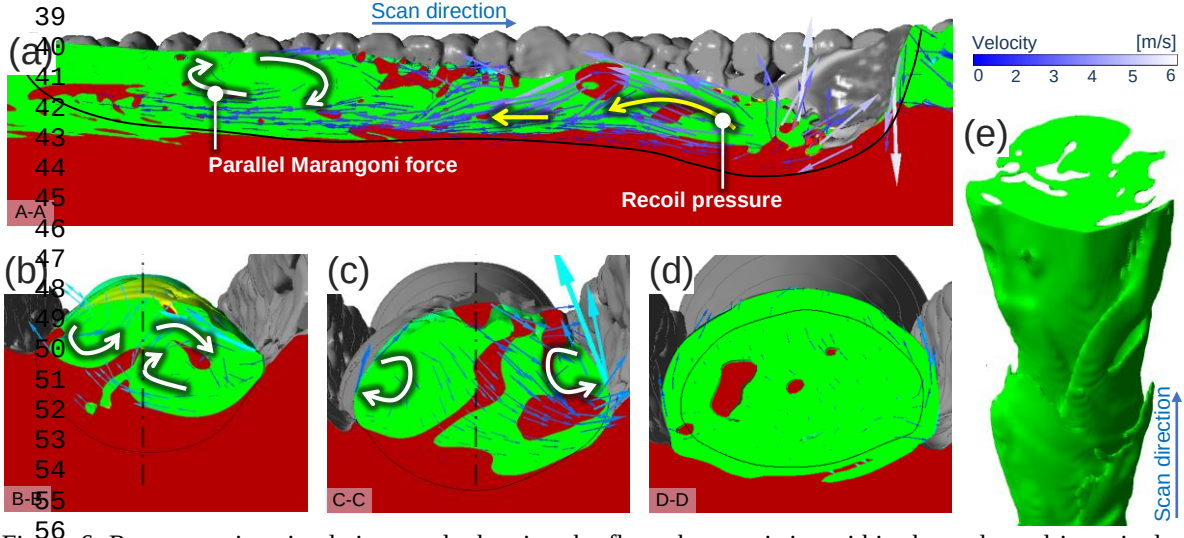

Figure 6. Representative simulation result showing the flow characteristics within the melt pool in a single track melt (L = 200 W, V = 1500 mm/s). Figures (a), (b), (c), and (d) are taken from the cross-sections A-A, B-B, C-C, and D-D illustrated in Figure 1. Color code: 316L – red; IN718 – green. Figure (e) shows the solidified alloy's interface that imaged from the viewing angle Ⅱ in Figure 1.

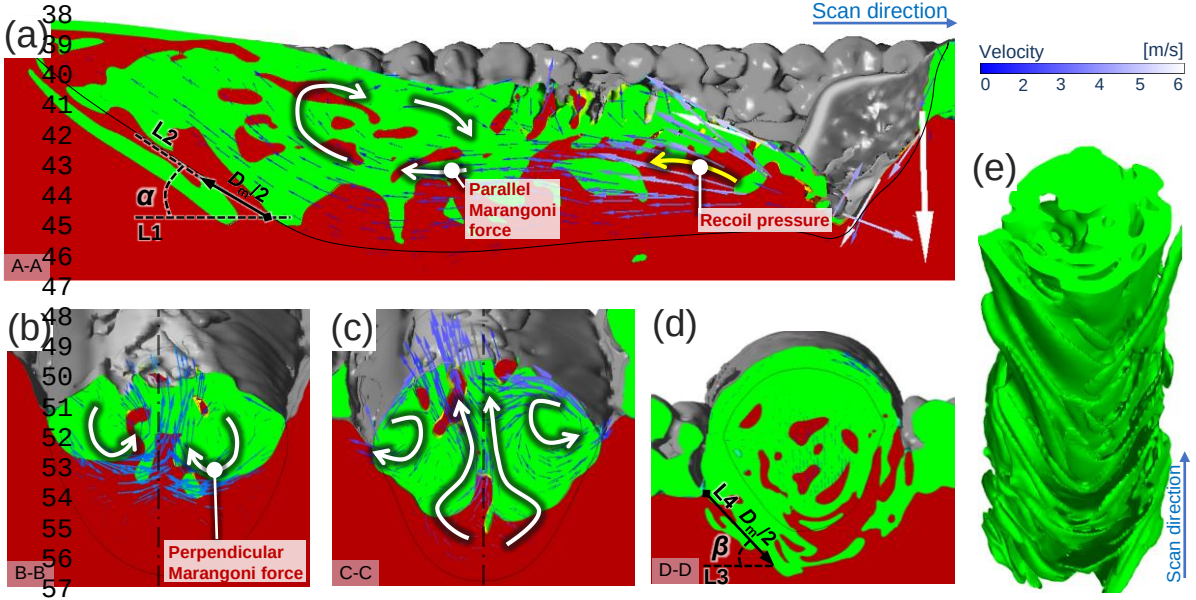

Figure 7. Representative simulation result showing the flow characteristics within the melt pool in a single-track melt (L = 200 W, V = 900 mm/s). Figures (a), (b), (c), and (d) are taken from the cross-sections A-A, B-B, C-C, and D-D illustrated in Figure 1. Color code: 316L – red; IN718 – green. Figure (e) shows the solidified alloy's interface that imaged from the viewing angle Ⅱ in Figure 1.

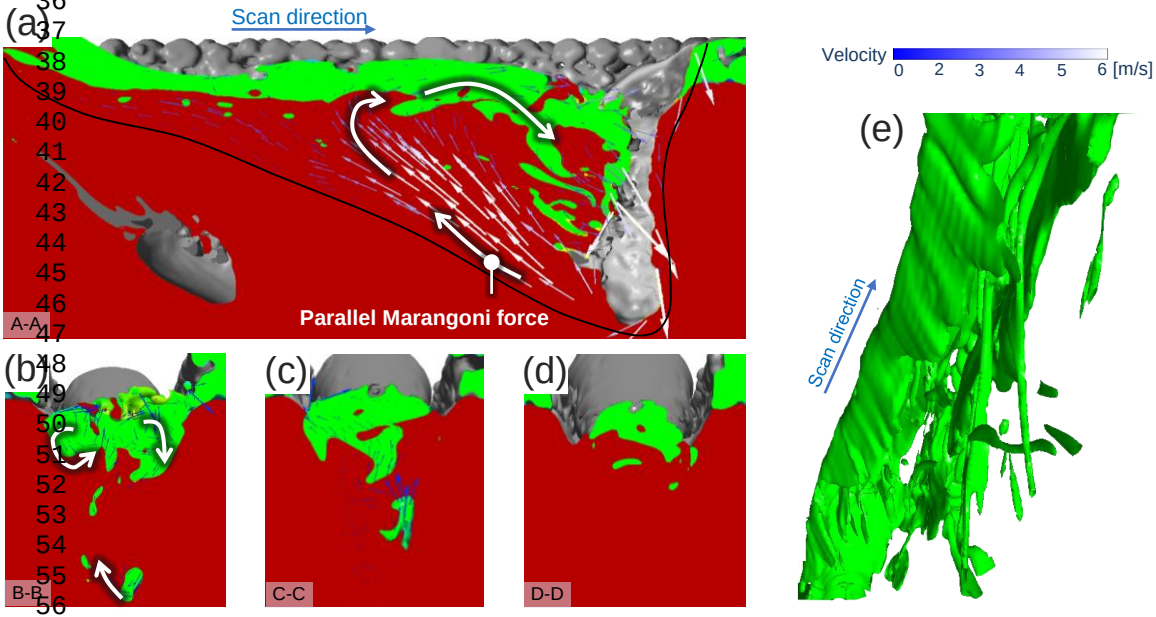

Figure 8. Representative simulation result showing the flow characteristics within the melt pool in a single-track melt (L = 200 W, V = 300 mm/s). Figures (a), (b), (c), and (d) are taken from the cross-sections A-A, B-B, C-C, and D-D illustrated in Figure 1. Color code: 316L – red; IN718 – green. Figure (e) shows the solidified alloy's interface that imaged from the viewing angle Ⅱ in Figure 1.

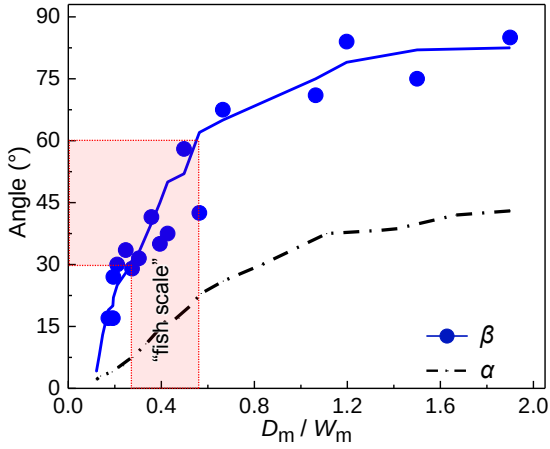

Figure 9. Variations of the melt pool boundary angles α and β with the melt pool aspect ratio D_m / W_m. Symbols are experimental results while the lines are from simulations. The transparent window in Figure corresponds to the processing window that produces independent "fish scales", which also exhibits moderate inter-diffusion (medium DoA) that is conducive for the formation of curved grains.

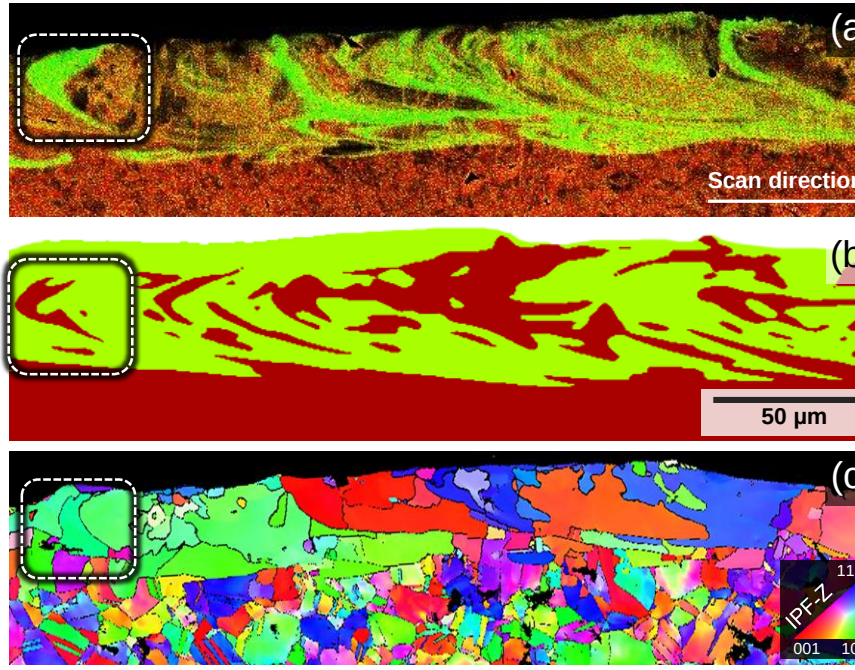

Figure 10. (a) Experimental elemental distribution map of Fe (red) and Ni (green) overlaid along the cross-section A-A obtained from the single-track laser scan with L = 100 W and V = 300 mm/s. Since Fe and Ni are the principal elements in 316L and IN718, respectively, the red and green regions can be taken to represent of 316L and IN718, respectively. (b) Corresponding simulated alloy distribution map (with red and green areas representing 316L and IN718, respectively.). (c) Corresponding grain orientation map obtained using EBSD. The dotted line boxes on the top-left region of (a), (b) and (c) highlight the 2D view of the fish scale formation, where curved grain can also be observed.

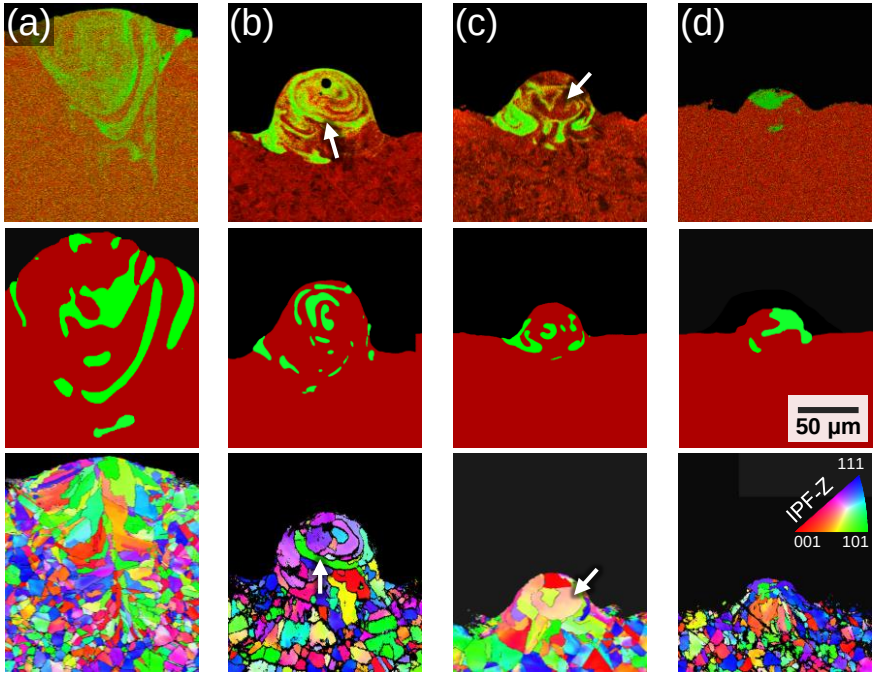

Figure 11. (Top row) Representative elemental distribution maps of Fe (red) and Ni (green) overlaid along the cross-section E-E (see Fig. 1) obtained from the single track laser scans with D_m / W_m of (a) 1.18, (b) 0.43, (c) 0.27, and (d) 0.23. (Middle row) Corresponding simulated results with the red and green regions representing 316L and IN718, respectively. (Bottom row) EBSD images showing the corresponding microstructures. The white arrows on the top row of Figures (b) and (c) indicate the formation of curved strips and swirls, and the white arrows on the bottom row of Figures (b) and (c) show the corresponding formation of curved grains.

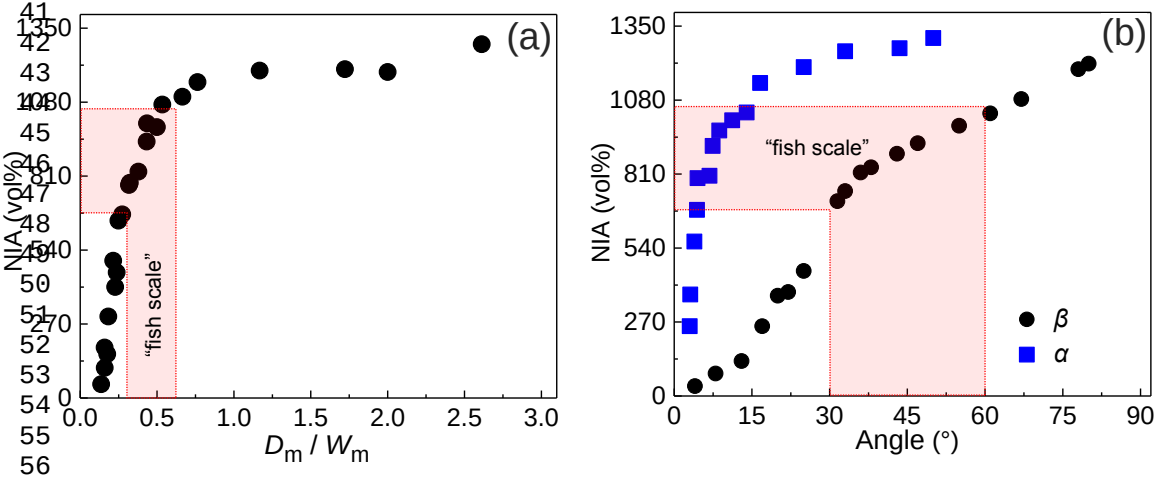

Figure 12. The impact of (a) D_m / W_m and (b) α, β on the normalized interfacial area (NIA). The transparent window in Figure corresponds to the processing window that produces independent "fish scales", which also exhibits moderate inter-diffusion (medium DoA) that is conducive for the formation of curved grains.

Graphical Abstract

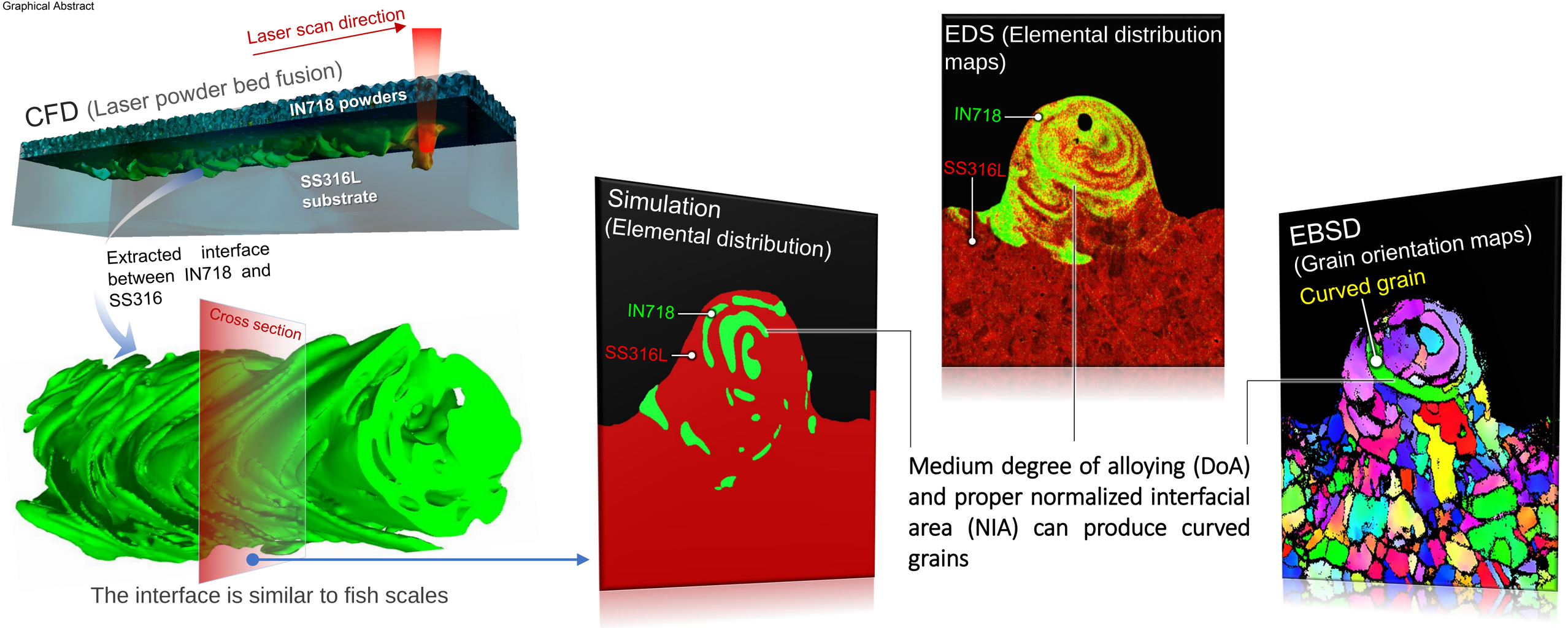

Click here to access/download

Video Still

Movie S1.mp4

Click here to access/download

Video Still

Movie S2.mp4

Click here to access/download

Video Still

Movie S3.mp4

Click here to access/download

Video Still

Movie S4.mp4

Click here to access/download

Video Still

Movie S5.mp4